

XMM–Newton Observation of the Cluster of Galaxies Abell 1650

Seiji TAKAHASHI and Koujun YAMASHITA

Department of Physics, Nagoya University, Furo-cho, Chikusa-ku, Nagoya 464-8602
takahasi@u.phys.nagoya-u.ac.jp

(Received 2003 July 31; accepted 2003 September 29)

Abstract

We present the nonuniform distribution of temperature and abundance in the angular extent of $10'$ (1.4 Mpc) in A 1650 observed by XMM-Newton. Spectral analysis was carried out in 19 systematically-subdivided regions, and in 15 specified regions referred to the hardness ratio (HR) map. The value of HR , defined as the ratio of counts in the 1.6–10 keV band to those in the 0.8–1.6 keV, is an indicator to investigate the spatial variation of spectral features. The temperature and abundance were obtained to be 4–6 keV and 0.2–0.5 solar value with average values of $5.62_{-0.07}^{+0.05}$ keV and $0.36_{-0.01}^{+0.02}$ solar value within a radius of $5'$, respectively. The redshift was derived to be $8.01_{-0.02}^{+0.02} \times 10^{-2}$ against an optical value of 8.45×10^{-2} . It turned out that cool regions with a temperature of around 4 keV and a scalelength of a few 100 kpc are patchily distributed in the outer envelope. This temperature structure could be explained by the infalling of groups of galaxies into the cluster main body. More than 30 point sources were found around A 1650 in the FOV of $30'$. The spectrum of the Galactic diffuse emission was obtained in the outskirts of A 1650.

Key words: galaxies: clusters: individual (Abell 1650) — galaxies: intergalactic medium — galaxies: evolution — X-rays: galaxies: clusters

1. Introduction

The structure and evolution of clusters of galaxies are considered in the scenario of gravitational infalling of groups of galaxies and the merging of clusters. The process may be described as a sequence of merging and relaxation phases in which substructures are alternatively accreted and merged into the larger system. N -body hydrodynamic simulations show that the merger of major cluster components produces pronounced nonuniformities of the plasma temperature, gas density, and magnetic field strength in an intracluster medium (ICM) (Roettiger et al. 1997; Roettiger, Flores 2000; Ricker 1998). Therefore, the temperature distribution in the ICM is sensitive to the processes of hierarchical clustering.

Previously, ASCA, ROSAT, and BeppoSAX demonstrated that many clusters have complex temperature structures in an ICM, suggesting that clusters have experienced a recent merger and are still forming (Markevitch et al. 1998; Furusho et al. 2001; Watanabe et al. 1999). Recent X-ray observations of XMM-Newton and Chandra enable us to study spatially resolved ICM X-ray spectra with excellent angular resolution and high sensitivity. The first observations show that the central regions of clusters are not simple spherically-symmetric systems, but are morphologically and spectroscopically very complex (e.g., A 2142: Markevitch et al. 2000; A 1795: Tamura et al. 2001; Sérsic 159-03: Kaastra et al. 2001; Centaurus: Sanders, Fabian 2002).

In this paper, we present the first XMM-Newton EPIC observation of the cluster of galaxies A 1650, which is characterized as a richness class 2, Bautz–Morgan type

I–II and optical redshift of $z = 0.0845$ (Abell et al. 1989; Struble, Rood 1999). Previous X-ray observations with Einstein (White et al. 1997), ROSAT (Peres et al. 1998), and ASCA (Ikebe et al. 2002; White 2000) have shown that A 1650 has an average temperature of approximately 6 keV, metallicities close to 0.3, an X-ray luminosity of 7.9×10^{44} erg s $^{-1}$ in the 0.1–2.4 keV band, contains a moderate cooling flow with a cooling rate of $\dot{M} = 280_{-80}^{+464} M_{\odot}$ yr $^{-1}$ and a cD galaxy 2MASXi J1258414–014541 in the center, which is radio quiet (Bagchi, Kapahi 1994).

Throughout this paper we assume $H_0 = 50$ km s $^{-1}$ Mpc $^{-1}$. One arcminute corresponds to 144 kpc at a redshift of 0.0845. We use the abundance measurements of Anders and Grevesse (1989) for spectral fitting, in which Fe/H = 4.68×10^{-5} by number. Errors are quoted at the 90% confidence level, unless otherwise stated.

2. Observation and Data Reduction

A 1650, located at $\alpha = 12^{\text{h}}58^{\text{m}}41^{\text{s}}5$, $\delta = -01^{\circ}45'41''4$ [J2000] (corresponding to galactic coordinates $l = 306^{\circ}68$, $b = 61^{\circ}06$), was observed for 43 ks by the XMM-Newton satellite (Jansen et al. 2001) in revolution 377 on 2001 December 29–30. The three EPIC cameras, MOS1, MOS2, and PN (Turner et al. 2001; Strüder et al. 2001) were operated in the full window mode with a medium filter.

We generated qualified event files using the standard tasks EMCHAIN and EPCHAIN in the XMM SAS version 5.3.3 software. X-ray events with patterns 0 to 12 for the

two MOS cameras were used, whereas for the PN single and double-pixel events were selected.

The light curve of this observation shows a partially and unusually high count rate due to the background induced by solar flares. During flares, the observed spectrum shows a hard continuum easily detectable above 10 keV. Therefore, we extracted the light curves over the whole field of view in the energy range of 10 to 15 keV, and then excluded all time intervals during solar flares. The selected events lead to effective exposure times of 37.1 ks, 38.1 ks, and 31.0 ks for the MOS1, MOS2, and PN cameras, respectively.

Blank-sky data sets were prepared from several pointings at high galactic latitude by removing point sources, and were used as background for all of this analysis. We applied the same screening criteria for the blank-sky backgrounds, which include the particle and sky background. CLOSED filter data were used for the particle background, and were normalized to derive the sky background while referring to the count rate in the energy band of 10 to 12 keV for MOSs and 12 to 14 keV for PN, because the particle background level is variable at about 10%. With this method, we corrected for the particle background. We also took into account the soft cosmic X-ray background (CXB), which depends on the viewing direction of the sky. To estimate the soft CXB, we used regions of the detector in which X-ray emission from the cluster was negligible. We extracted a spectrum in the annulus between $10'$ and $15'$ from the cluster center, excluding bright point sources, and derived the normalization factor between the blank-sky fields and A 1650 observations. The CXB in blank-sky fields and around A 1650 in the soft band (0.5–3.0 keV) differ by less than 3%. We thus used the above normalization factor. Background spectra have been accumulated from the same detector areas as the source spectra.

Finally, a vignetting correction was applied to the event files by using a method proposed by Arnaud et al. (2001). Bright streak pixels for both MOSs and PN, and the pixels with high electric noise close to CCD border for PN were masked out manually.

3. Cluster Morphology

The whole X-ray image in the field of view was constructed in color-coded energy bands of 0.3–1.3 keV (red), 1.3–2 keV (green), and 2–10 keV (blue) by combining MOSs and PN event files with a pixel size of $4''.4$, as shown in figure 1. The effects of out-of-time events can be seen as a thin luminous band in the lower chip, fourth from the left.

The X-ray color image represents the surface brightness distribution and spectral feature. Soft sources appear red, moderately hard sources appear green, and the hardest sources appear blue. The angular size of A 1650 seems to extend to a radius of $10'$. Therefore, we show an X-ray surface brightness distribution in the 0.8–10 keV band from the two weighted MOS event files with a pixel size of $4''.4$ and a Gaussian filter with $\sigma = 4''.4$ in a $10' \times 10'$ region

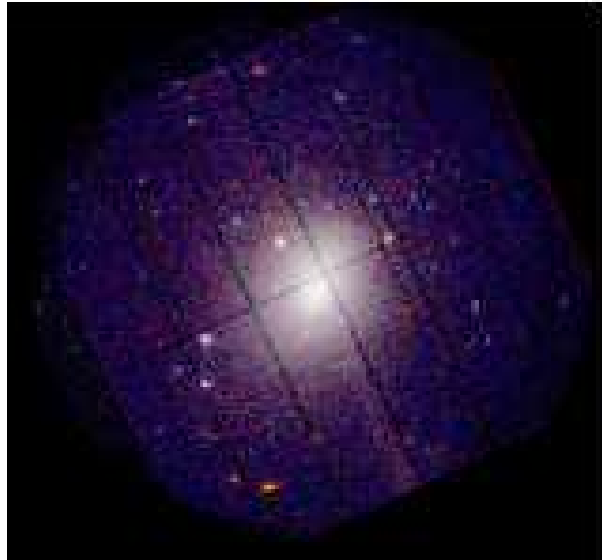


Fig. 1. X-ray color image combining MOSs and PN of the central $30' \times 30'$ of A 1650. The red, green, and blue intensities correspond to counts from energy bands of 0.3–1.3 keV, 1.3–2.0 keV, and 2.0–10.0 keV respectively. The lines are due to the gaps between CCD chips.

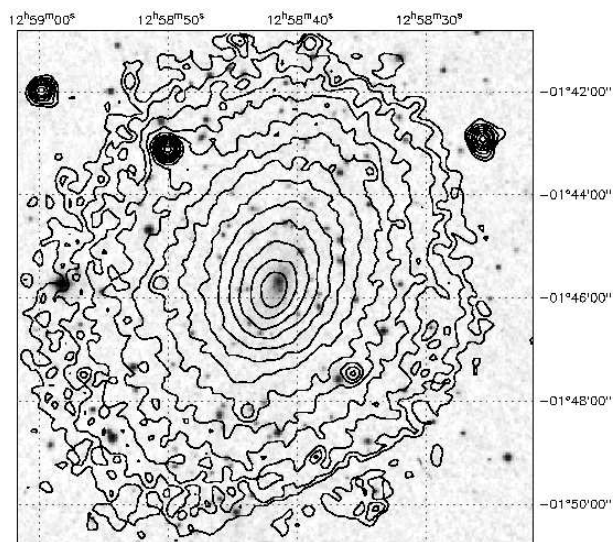


Fig. 2. MOSs X-ray surface brightness contours logarithmically spaced by a factor of $\sqrt{2}$, binned by $4''.4$ pixels and filtered with a $\sigma = 4''.4$ Gaussian in the 0.8–10 keV band after subtracting background, overlaid on the Digitized Sky Survey optical image. The field is $10' \times 10'$ with north up and east to the left. The linear artifacts are due to the gaps between CCD chips.

centered on the brightness peak and overlaid on the DSS optical image in figure 2. The X-ray morphology of A 1650 is centrally concentrated and slightly elongated with an elliptical shape and a position angle of $\sim 20^\circ$ (north to west). The optical center of the cD galaxy and the peak position of the X-ray surface brightness are displaced by about $10''$ (23 kpc) toward the southeast. The orientation of cD galaxy is well-aligned to that of the cluster.

There is no clear evidence of substructures, suggesting that the cluster has not experienced a major merger in the recent past, and is in a relaxed state. To identify significant substructures in the core, we fitted the combined MOSs image with a 2D elliptical β -model and built up a map of the residuals of the data over the best-fit model. Images were extracted in the 0.8–10 keV band from the weighted MOS event files in a pixel of size $4'' \times 4''$, and added to make a combined MOS image. We fit the image within an angular radius of $8'$, excluding bright point sources and the region close to the CCD border. We fixed the centroid parameters to the X-ray emission peak, and allowed the core radius r_c , index β , ellipticity ϵ , position angle PA and normalization n_0 to vary. The best-fit elliptical β -model, $n = n_0[1 + (r/r_c)^2]^{-3\beta/2}$, yields a core radius, r_c , of $0''.86$ (123 kpc), a β of 0.57, an ϵ of 0.26, and a PA of -22.0° .

The color-coded significance of the excess image with contours spaced by 0.5 after Gaussian smoothing with $\sigma = 4'' \times 4''$, are shown in figure 3. We can unambiguously confirm the excess emission around the central cD galaxy and the excess of diffuse gas in the direction to north. The image deficiency in south from the center is a kind of artifact reflecting a steeper gradient of the surface brightness distribution and compensating the excess in north shown in figures 2 and 3, which depends on the position of the image center and the angular range of the radial profile fitting. This surface brightness distribution is similar to that of A 2142 (Markevitch et al. 2000).

In addition, with XMM-Newton's high angular resolution ($15''$ HPD) and good statistics, we could easily recognize three bright X-ray sources in the northern part, and resolve four point sources at radii of $2' - 3'$ from the center. Although some of them were identified as optical and radio sources, there were no measurements of their optical redshift. Therefore, we do not know whether these point sources are associated with the cluster or not.

4. Spectro-Imaging Analysis

We studied the spatially-resolved spectral feature using a hardness ratio (HR) map. Since the XMM-Newton telescope PSF has a very weak energy dependence, we simply considered the spectral variation from the X-ray hardness ratio. We defined $HR = I(1.6-10 \text{ keV})/I(0.8-1.6 \text{ keV})$ as the ratio of the counts in the respective energy bands, so that the counts in each energy band were almost the same in order to minimize statistical error. The value of HR is not only a temperature indicator, but also an absorption measure, and the mixture of complex spectral components. These properties could be confirmed by a spectral analysis in the respective regions re-

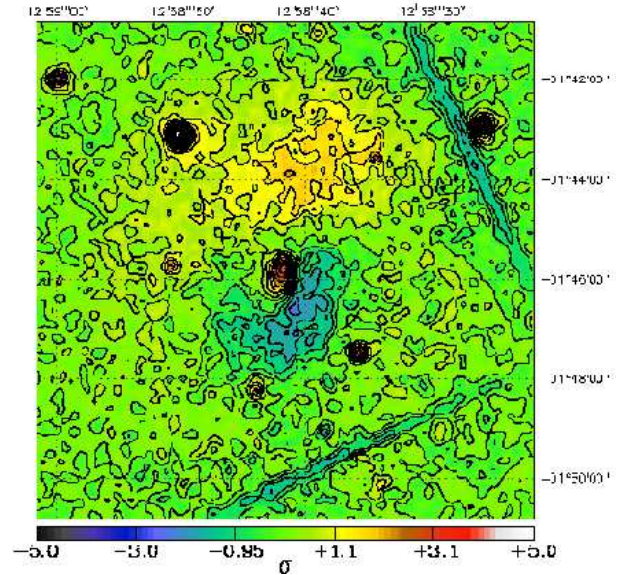


Fig. 3. Color-coded image in 0.8–10 keV with contours spaced by 0.5 corresponds to the residuals after subtraction of the 2D elliptical β -model, smoothed with $4'' \times 4''$ Gaussian profile.

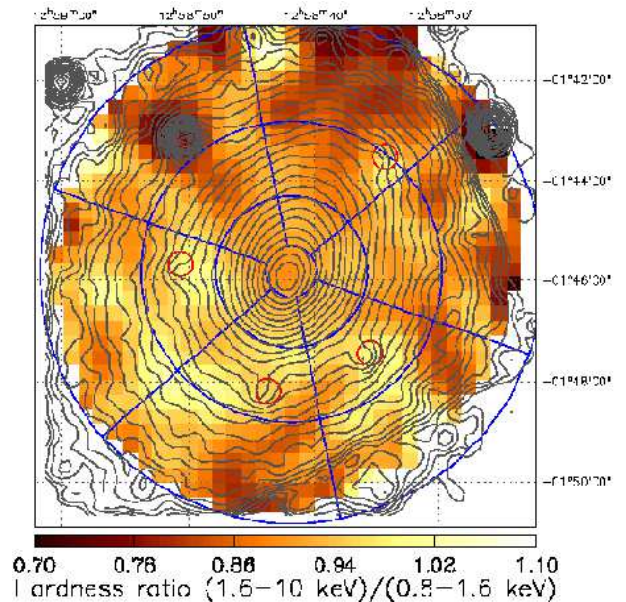


Fig. 4. Color-coded hardness ratio map overlaid on the X-ray surface brightness distribution, obtained by MOSs. The contours are logarithmically spaced by a factor of 1.20, binned by $8'' \times 8''$ pixels and filtered with a $\sigma = 8'' \times 8''$ Gaussian profile in the energy band of 0.8–10 keV. The field is $10' \times 10'$ with north up and east to the left. HR map is binned by $17'' \times 17''$ pixels and filtered with a $\sigma = 21'' \times 21''$ Gaussian and shown in gray scale in the diameter of $10'$. The temperature and abundance for these 18 sectors are given in figure 8. Red circles indicate point sources.

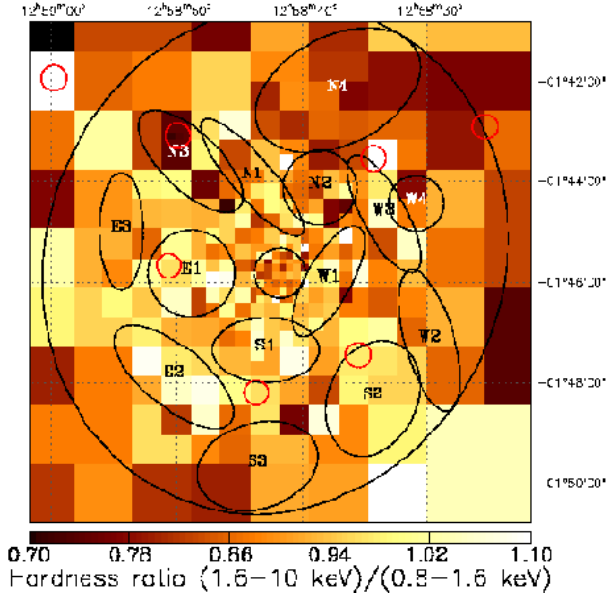


Fig. 5. Color-coded adaptively binned hardness ratio map with a fractional error of 0.10 in the same field as figure 4. The encircled regions with an identification mark were selected for a spectral analysis. The positions of seven point sources in figure 4 are indicated by red circles.

ferred to the HR map. Based on a single-temperature assumption, the relation between the HR values and the temperature (kT) can be approximately expressed as $HR = 0.131 + 0.906 \times (kT/5.62 - 0.387)^{0.294}$. $HR = 1$ corresponds to $kT = 7$ keV. Because the fractional errors of HR s are twice as large as those of the surface brightness distribution in the 0.8–10 keV band, the pixel sizes of the HR s were adjusted to obtain comparable statistics to the surface-brightness distribution.

Figure 4 shows an HR map with values in the range of 0.7–1.1 overlaid on X-ray surface brightness contours for a diameter of $10'$ centered on the brightness peak by using MOSs data. These images were binned by $8''.8$ pixels and filtered with a $\sigma = 13''.2$ Gaussian for the surface brightness contour and $17''.6$ pixels and filtered with a $\sigma = 21''.1$ Gaussian for the HR map. The systematically divided sector pattern is overlaid on this map, which defines regions for another spectral analysis to compare the HR map.

Smaller bin sizes too much exaggerate any small-scale fluctuation in the outer region, while larger ones smear out the significant structure in the central region, and statistically clarify the structure in the outer region. In order to show the overall feature in one figure, we used an adaptive binning routine (Sanders, Fabian 2001) to produce the HR map. Although the physical scale changed in this method, we ensured comparable fractional errors per bin in each band. We defined the same HR and produced HR with a fractional error of 0.10, as shown in figure 5. The minimum pixel size is $8''.8$ in the central region and the maximum one is $1/2$ in the outer region. The overall feature is similar to the HR map in figure 4. The en-

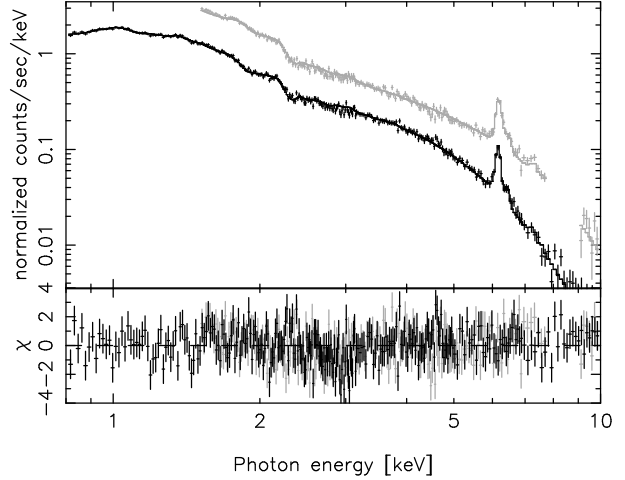


Fig. 6. Energy spectra of the MOSs (lower) and PN (upper) in the radius of $5'$. The solid lines indicate the best-fit isothermal model with $kT = 5.62$ keV, an abundance of 0.36 times the solar value, and a redshift of 0.0801.

circled regions with an identification mark (N1, S1, ...) were selected for the further spectral analysis mentioned in subsection 5.3.

There exist significantly cool regions and a scalelength of a few 100 kpc, patchily distributed in the outer envelope. At larger scales, the maps show that the hotter cluster gas lies southeast of its brightness peak and cooler gas lies northwest, coinciding with the excess structure, as shown in figure 3. The maps also shows that the cluster brightness peak is moderately cool.

5. Spectral Analysis

5.1. Overall Cluster Spectrum

The overall spectra of MOSs and PN were accumulated from all events within a radius of $5'$, which included most of the cluster emission and excluded obvious point sources. Each overall spectrum was fitted with MEKAL, a collisionally ionized thermal plasma model (Mewe et al. 1985, 1986; Kaastra 1992; Liedahl et al. 1995), incorporated with the absorption of Galactic neutral gas. We excluded the energy bins around the strong instrumental fluorescence lines of Ni, Cu, and Zn in the energy range 7.8–9.0 keV from the PN spectral fitting. These lines were not consistently subtracted from source spectra, since they were not linearly related to the continuum of the particle-induced background. All spectral fittings were performed using version 11.2.0 of the XSPEC package.

The amount of absorption is fixed at a Galactic value of $N_H = 1.56 \times 10^{20} \text{ cm}^{-2}$ (Dickey, Lockman 1990). The centroid energies of the Fe-K α are systematically larger than the value estimated from the optical redshift of 0.0845 (Struble, Rood 1999). Thus, the redshift was also allowed to vary. We obtained the best-fit with a redshift of $7.95^{+0.12}_{-0.11} \times 10^{-2}$ for MOSs and $8.01^{+0.20}_{-0.17} \times 10^{-2}$ for PN. Since the MOSs and PN spectra are consistent within the error bars, we adopted a value of 0.0801, derived from

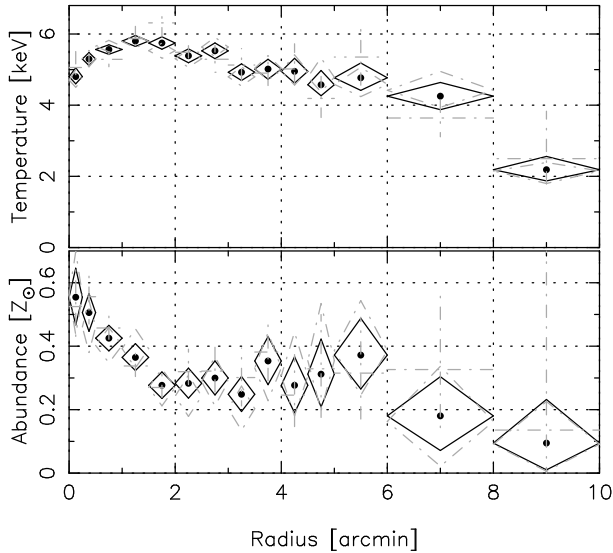


Fig. 7. Top: Radial temperature profile of A 1650 as a function of angular radius. Bottom: Radial abundance profile. The solid diamonds show the results of a combined fitting of MOSs and PN spectra. For a comparison, individual values of MOSs (dash-dotted diamonds) and PN (dash-dotted crosses) are also shown.

a simultaneous fit of MOSs and the PN spectra as the redshift of A 1650.

There is also inconsistency for the temperature derived with the MOS and PN data over the whole energy region of 0.3–10 keV. This can be due to the soft component in the sky, noticed by Nevalainen et al. (2003), or an artifact due to remaining calibration uncertainties. Therefore, we investigated the influence of various low-energy cutoffs upon the temperature and abundance for each instrument. It was found that there is an optimum low-energy cutoff for each instrument, above which an even higher cutoff energy will not significantly alter the resulting temperature. The temperatures derived from MOSs and PN are consistent, and the converge above the cutoff energy, which is 0.8 keV for the MOSs and 1.5 keV for the PN data.

Consequently, we restricted our fit to the 0.8–10 keV energy band for MOSs and 1.5–10 keV energy band for PN. The spectra were corrected for vignetting and background subtracted, shown in figure 6. The best-fit values of temperature (kT) and abundance (Z) are $5.62^{+0.05}_{-0.07}$ keV and $0.36^{+0.02}_{-0.01}$ solar for MOSs+PN respectively as listed in table 1. The observed flux in 2–10 keV is 1.9×10^{-11} erg s^{-1} cm^{-2} , corresponding to a luminosity of 5.6×10^{44} erg s^{-1} . We also analysed the ASCA GIS spectra in the 0.7–10 keV band, and obtained $kT = 5.84^{+0.19}_{-0.17}$ keV and $Z = 0.36^{+0.06}_{-0.06}$ solar, which are consistent with the above-mentioned values. We adopted the low-energy cutoffs thus derived for the spatially-resolved spectral analysis discussed below, unless otherwise stated.

5.2. Radial and Azimuthal Profiles of Temperature and Abundance

We produced a radial temperature profile by excluding obvious point sources and extracting spectra in annuli centered on the peak of the X-ray emission. We extracted spectra in fourteen concentric annular regions out to $10'$. Combined MOSs and PN spectra were binned to at least 20 counts to allow the use of Gaussian statistics.

Each vignetting corrected and background-subtracted spectrum of MOS and PN was then fitted simultaneously with an isothermal MEKAL model, allowing the normalization, temperature and abundance to be free parameters. In figure 7 we show the radial profile of the projected emission-weighted temperature and abundance. We can recognize the obvious drop of temperature down to 4.8 keV in the core. This spectral feature corresponds to the image excess at the center shown in figure 3. Furthermore, temperatures gradually decrease beyond about $2'$ and steeply drop down in $8'$ – $10'$.

Figure 7 also shows the profile derived in the conservative radial range where we have information from the Fe-K α line. We observe 0.3 solar abundances outside of $r = 2'$ and a very sharp increase in the core to 0.55 solar. The average abundance is 0.36, more typical of the value found by De Grandi and Molendi (2001) for cooling flow clusters (0.34 ± 0.01). The profile exhibits a three phase behavior, rather than a steadily declining profile. It decreases up to $r = 3'$, and increases at a more or less constant rate with a mean of 0.35 up to $r = 6'$ and decreases again. Irwin and Bregman (2001) showed that the abundance profiles of A 1795, A 2142, and A 2163 clusters are also not monolithically declining with the radius.

In order to further investigate the spatial distribution of the temperature and abundance, we systematically divided the region within $r = 5'$ into 19 regions with $r = 0'.5$, $1'.5$ and $3'$ and 6 sectors in the azimuth except for $r < 0'.5$, as shown in figure 4. The same procedure of spectral fitting was applied to each region. The results are shown concerning the relation of the temperature and abundance in figure 8. It is noticed that at $r = 0'.5$ – $1'.5$ the abundances azimuthally vary in the range of 0.31–0.46 solar at an almost constant temperature of 5.6 keV, whereas at $r = 1'.5$ – $3'$, the temperatures increase up to 6.1 keV with nearly constant abundances and at $r = 3'$ – $5'$ the temperatures are shifted down to 4.4 keV with a slight variation of the abundances.

5.3. Spectra in Characteristic Regions

We chose 15 characteristic regions excluding obvious point sources, as identified in figure 5, in which the spectra were analysed to quantify the statistical significance of the spectral features in the HR map. We performed a spectral fitting with a single temperature MEKAL model. The free parameters were the normalization, temperature, and abundance, fixing N_H to the Galactic value. The total counts used for the spectral fitting in selected regions were in the range of 2000–12000/region, depending on the size of the regions and the radial position angle on the

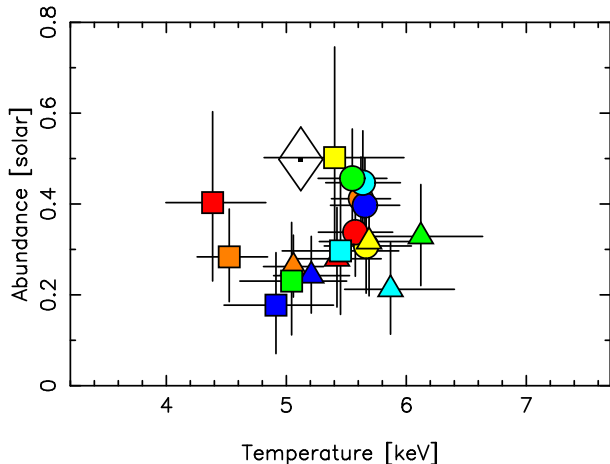


Fig. 8. Best-fit values of the temperature and abundance obtained by the MOSs spectra in 19 systematically divided regions, shown in figure 4, as a radial pattern. The marker styles and colors indicate the radial positions, and position angles, respectively. Diamond: $r < 0'.5$, filled circle: 6 sectors in $r = 0'.5-1'.5$, filled triangle: 6 sectors in $1'.5-3'$, filled square: 6 sectors in $r = 3'-5'$. Orange: $-50^\circ - 10^\circ$ (north), red: $10^\circ - 70^\circ$ (northeast), yellow: $70^\circ - 130^\circ$ (southeast), green: $130^\circ - 190^\circ$ (south), light blue: $190^\circ - 250^\circ$ (southwest), blue: $250^\circ - 310^\circ$ (northwest), where the angles are measured from north through east.

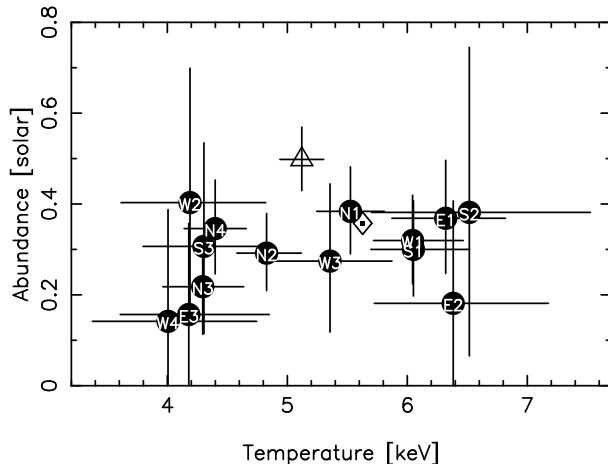


Fig. 9. Best-fit values of the temperature and abundance in selected regions with identification marks shown in figure 5. Diamond, mean values in $r < 0'.5$; triangle: in $r < 0'.5$.

surface-brightness distribution. Errors were assigned with the 90% confidence level for single parameters. The best-fit values of the temperature and abundance thus obtained are plotted in figure 9, which are varied in the range of 4–6 keV, corresponding to HR values of 0.78–1.0 and 0.15–0.55 solar, respectively.

We find a temperature of 5.12 keV and an abundance of 0.50 solar in the central region ($r < 0'.5$), as listed in table 1 and shown in figure 9 with the triangle mark. The calculated radiative cooling time is below the Hubble time in the center. Therefore, we also fitted an absorbed thermal (MEKAL) plus cooling flow (MKCFLOW) model to this region. The mass-deposition rate within $r = 0'.5$ is $3_{-3}^{+5} M_\odot \text{ yr}^{-1}$. Adding a cooling flow component does not provide any improvement to the fit.

The lower values of temperature around 4 keV were obtained in regions of N3, N4, E3, S3, W2, and W4. Region S2 shows the maximum value of the temperature. Regions N1 and W3 are close to the average value. It is obvious that the HR values are well correlated to temperatures obtained from the spectra. Referring to figure 9, selected regions are divided into 3 groups: high temperature group (E1, S1, S2, W1), low temperature and high abundance group (N4, S3, W2) and low temperature and low abundance group (N3, E3, W4). The spectra in these groups were fitted with the MEKAL model; the best-fit parameters are listed in table 1.

5.4. Galactic Diffuse Emission

The MOS spectrum of the outskirts of A 1650 in $r = 10'-15'$ was fitted with the model spectra of MEKAL and the cosmic X-ray background. The MEKAL model corre-

sponds to the Galactic diffuse emission. The CXB model was fixed as a power-law (photon index of 1.4) incorporated with the Galactic N_H value in this direction. We used data sets taken with the CLOSED filter position for background subtraction, and excluded the fluorescent emission line of Al-K α in the energy range of 1.35–1.6 keV from the fitting. The result is shown in figure 10. We can clearly recognize strong emission lines of O VII (0.57 keV) and O VIII (0.65 keV), which result in an oxygen abundance of $0.099_{-0.006}^{+0.010}$ solar with a temperature of $0.211_{-0.008}^{+0.006}$ keV. The depleted oxygen abundance is not consistent with the previous picture of the hot interstellar medium (Hayakawa et al. 1978), which indicates that metallic elements are depleted by trapping in dust grains, whereas the oxygen abundance is similar to the solar value. The galactic diffuse soft X-ray spectrum could be explained by a low-temperature component ($kT = 0.1$ keV) from a local hot bubble surrounding the solar system and extending to 100 pc or so, and a high-temperature one ($kT = 0.2-0.3$ keV) associated with radio loops and other enhanced regions. Using two temperature model, we tried to fit the observed spectrum, since A 1650 is located in the high galactic latitude and in the direction of a part of Loop I (Snowden et al. 1995). We obtained a slightly better fitting with $kT = 0.11$ and 0.24 keV and abundance of 0.9 solar, though the coupling of parameters was rather strong. This problem should be further investigated using data obtained with XMM-Newton observations.

6. Point Sources

Unexpectedly, many sources were observed around A 1650, which were not found in the ASCA X-ray image. Ten bright point sources shown in figure 11 are listed in table 2 with coordinates, net counts, spectral indices, N_H values, χ^2_v/dof and fluxes in the 2–10 keV band. Source spectra were extracted from circular regions of $0'.25$ radius for MOSs and PN. Background spectra were taken from

Table 1. Best-fit parameters of the spectral fitting*.

Region	Instrument	kT	Z	Redshift	χ^2/dof	HR	Net counts [†]
		(keV)	(solar)	($\times 10^{-2}$)			
$r < 5'$	MOSs	$5.62^{+0.08}_{-0.07}$	$0.35^{+0.02}_{-0.02}$	$7.95^{+0.12}_{-0.11}$	328.4/272	0.93	182684
	PN	$5.60^{+0.10}_{-0.07}$	$0.37^{+0.02}_{-0.02}$	$8.01^{+0.20}_{-0.17}$	280.4/214	...	96459
	MOSs and PN	$5.62^{+0.05}_{-0.07}$	$0.36^{+0.02}_{-0.01}$	$8.01^{+0.02}_{-0.02}$	609.3/487	...	279143
$r < 0.5'$	MOSs	$5.12^{+0.18}_{-0.18}$	$0.50^{+0.07}_{-0.07}$...	280.1/272	0.89	23062
	PN	$5.13^{+0.26}_{-0.25}$	$0.54^{+0.07}_{-0.07}$...	229.8/214	...	13106
	MOSs and PN	$5.14^{+0.14}_{-0.15}$	$0.52^{+0.05}_{-0.05}$...	508.8/488	...	36168
N4+S3+W2	MOSs	$4.45^{+0.21}_{-0.21}$	$0.34^{+0.09}_{-0.08}$...	293.0/272	0.85	12634
N3+E3+W4	MOSs	$4.55^{+0.37}_{-0.28}$	$0.16^{+0.09}_{-0.08}$...	205.7/193	0.84	8068
E1+S1+S2+W1	MOSs	$6.02^{+0.25}_{-0.19}$	$0.32^{+0.05}_{-0.05}$...	318.3/272	0.99	36064

* PN data are partially masked out to avoid hot pixels near CCD boundary.

† Net counts are summed up in 0.8–10 keV for MOSs and 1.5–10 keV for PN.

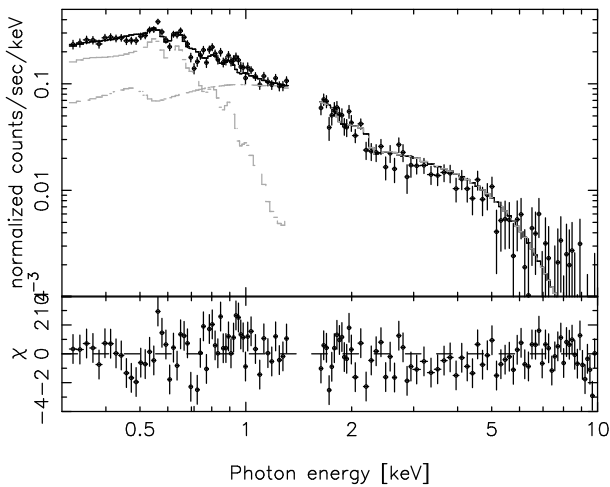


Fig. 10. Galactic diffuse and CXB spectrum derived from MOS data in the angular region of $r = 10' - 15'$ free from the contribution of A 1650. The dashed line represents the MEKAL model for the Galactic thermal component, while the dash-dotted line represents the power-law model with $\Gamma = 1.4$ and $N_H = 1.56 \times 10^{20} \text{ cm}^{-2}$ for CXB. The solid line is their combination.

identical circular source-free regions in the vicinity of each source. We fit the model to all three datasets between 0.3 and 10 keV simultaneously, and the spectra were grouped to have a minimum of 20 counts in each bin. Their spectra, subtracting the diffuse cluster component, were fitted by a power-law model, except for S8, since significant emission lines were not recognized in their spectra. The best-fits to the spectra of S0 and S5 are shown in figure 12, demonstrating that S5 requires substantial amounts of excess absorption.

S0 is the brightest object, and is located at a radius of $3/35$ from the cluster center. The peak intensity is almost comparable to that of the cluster center. This angular separation and intensity make it possible to detect with the ASCA observation. This means that S0 would be highly variable. The 0.3–10 keV spectrum is featureless and well fitted by a power-law with a photon index of $2.15^{+0.07}_{-0.04}$ ($\chi^2/\text{dof} = 289.0/305$), as shown in figure 12.

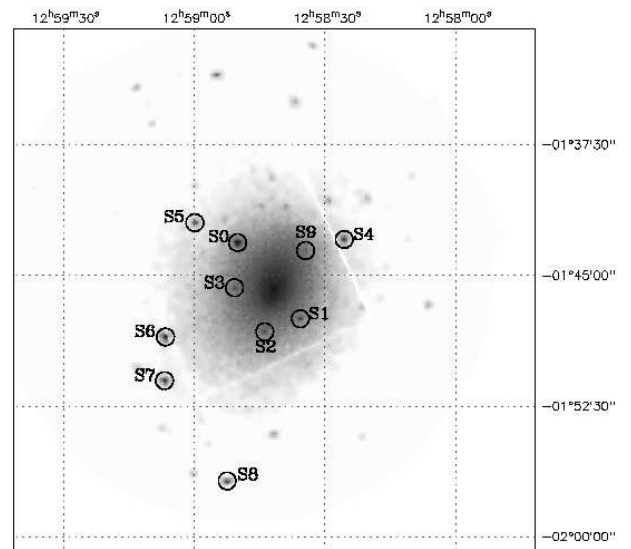


Fig. 11. Adaptively smoothed broadband (0.3–10 keV) MOSs image of the $30' \times 30'$ region surrounding the center of A 1650. The open circles correspond to the bright point sources given in table 2.

A thermal plasma model fits it poorly. The spectrum of S0 is similar to the steep spectra found in BL Lac objects (Cileigi et al. 1995). S1, S2, S3, and S9 are located within a radius of $2' - 3'$. Since the spectra of AGNs are rather homogeneously represented by a power-law with a photon index of 1.7–2.0 (Nandra, Pounds 1994), S1, S2, S3, and S9 may be AGNs. S5 shows the strong intrinsic absorption caused by the surrounding matter of the source. The intrinsic absorption inferred from spectral fits is $4.14^{+1.49}_{-1.77} \times 10^{21} \text{ cm}^{-2}$ and the photon index is $1.72^{+0.17}_{-0.30}$. This amount of absorption and the photon index imply that S5 is an obscured AGN. S7 is a bright radio source (PKS 1256–015). S8 is identified with a star (HD 112719), and shows a thermal spectrum. If Fe-K α lines could be found in the spectra, we could estimate the redshift. Because optical identification of these objects is rather poor, we have to investigate them further.

Table 2. Characteristics of point sources.

ID	R.A. (J2000.0)	Decl. (J2000.0)	Net counts*	Γ^\dagger	N_H ($\times 10^{21} \text{cm}^{-2}$)	χ^2_ν/dof	$F_X(2\text{--}10 \text{keV})$ ($\text{erg s}^{-1} \text{cm}^{-2}$)	Comments
S0	12 58 49.92	-01 43 04.5	7729	$2.15^{+0.07}_{-0.04}$	$0.00^{+0.10}_{-0.00}$	289.0/305	21.09×10^{-14}	
S1	12 58 35.52	-01 47 26.4	1433	$1.93^{+0.14}_{-0.09}$	$0.00^{+0.14}_{-0.00}$	100.6/96	10.66×10^{-14}	
S2	12 58 43.68	-01 48 11.4	677	$2.28^{+0.69}_{-0.57}$	$2.01^{+2.33}_{-1.53}$	116.5/100	3.19×10^{-14}	
S3	12 58 50.64	-01 45 39.9	672	$1.82^{+0.37}_{-0.21}$	$0.00^{+0.42}_{-0.00}$	106.7/101	3.30×10^{-14}	
S4	12 58 25.44	-01 42 53.6	1395	$2.11^{+0.26}_{-0.14}$	$0.20^{+0.46}_{-0.20}$	64.7/76	6.22×10^{-14}	
S5	12 58 59.76	-01 41 55.9	727	$1.72^{+0.17}_{-0.10}$	$4.14^{+1.49}_{-1.77}$	46.6/43	7.99×10^{-14}	EXSS 1256.5-0134
S6	12 59 06.48	-01 48 29.3	3440	$1.83^{+0.10}_{-0.08}$	$0.31^{+0.19}_{-0.16}$	166.0/160	22.06×10^{-14}	
S7	12 59 06.72	-01 50 59.5	1941	$1.77^{+0.20}_{-0.09}$	$0.15^{+0.45}_{-0.14}$	92.3/93	14.74×10^{-14}	PKS 1256-015
S8	12 58 52.32	-01 56 45.0	1252	$0.53^{+0.05}_{-0.03}$	$0.12^{+0.03}_{-0.03} Z_\odot$	60.3/54	0.24×10^{-14}	HD 112719
S9	12 58 34.32	-01 43 31.7	590	$1.50^{+0.59}_{-0.22}$	$0.38^{+0.16}_{-0.38}$	70.3/84	4.97×10^{-14}	

* Net counts in $r < 0.25'$ from the center of each source and in 0.3–10keV.

† Results of the power-law fits except for S8 which is fitted with MEKAL model.

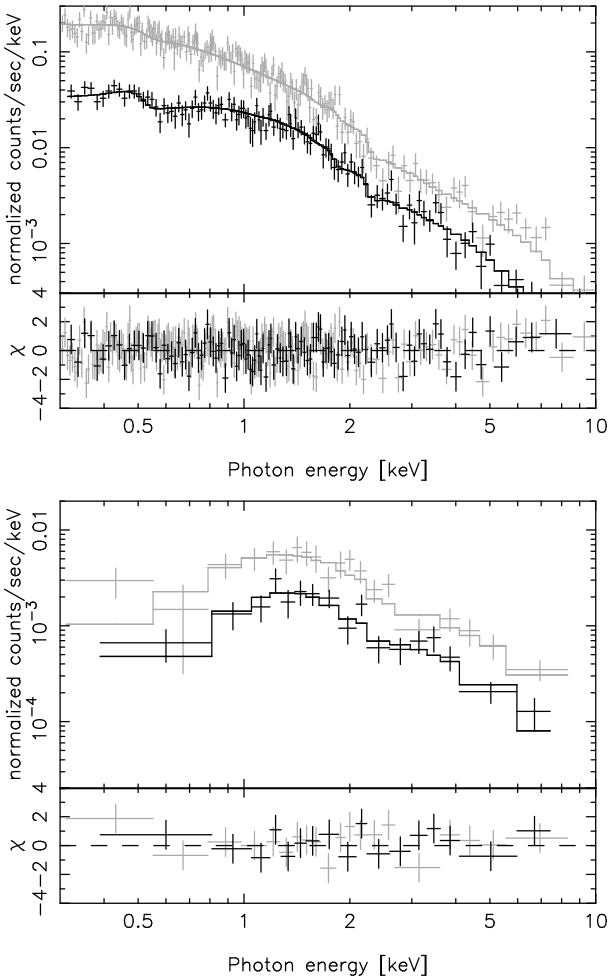


Fig. 12. Top: MOSs (lower) and PN (upper) spectra of S0 with the best-fit model (a power-law with $\Gamma = 2.15^{+0.07}_{-0.04}$ modified by the Galactic absorption). Bottom: Those of S5 with the best-fit intrinsic absorption model (an absorbed power-law with $\Gamma = 1.72^{+0.17}_{-0.30}$ and $N_H = 4.14^{+1.49}_{-1.77} \times 10^{21} \text{cm}^{-2}$)

7. Discussion

The overall spectrum of A 1650 is well-expressed with a single-temperature model, which indicates that this cluster is isothermal and relaxed. It is not easy to find the multi temperature components only from a spectral fitting. The spectral analysis referring to the HR map makes it possible to spatially distinguish several temperature components of 4–6 keV and the 0.2–0.5 solar abundance from the overall spectrum. This fact is also confirmed by a spectral analysis in the systematically sub-divided regions. The HR map more clearly shows the distribution of temperature components, as shown in figure 9.

There exist significantly cool regions with a temperature of around 4 keV and a scalelength of a few 100 kpc patchily distributed in the outer envelope. Also, somewhat hot regions with a temperature of around 6 keV are extended in the southeast direction. Some of point sources are located in the hot region. The central region within a radius of $0.5'$ obviously shows a lower temperature and a higher abundance compared to the average values within a radius of $5'$, which seems to be related to the existence of a cD galaxy. The image excess region extended to the north in figure 3 shows a lower temperature of 5 keV.

The characteristic time, $\delta\tau$, required to smear out the electron temperature gradient and arising from the effect of the thermal conduction alone would be $\delta\tau = \delta r / \bar{v} = \delta r / (\frac{2}{3} \frac{\kappa}{n_e k T_e} \frac{d(kT_e)}{dr})$ (Spitzer 1962). We adopted typical values of $n_e = 5.0 \times 10^{-3} \text{cm}^{-3}$ and $\Delta T_e = 1.0 \text{keV}$. Assuming that the scalelength, δr , of this temperature gradient is 50 kpc, the diffusion timescale, $\delta\tau$, is estimated to be $3 \times 10^8 \text{yr}$, shorter than the expected age of the cluster. We discuss several possible explanations for this temperature structure.

We could see no evidence for a large-scale temperature variation and X-ray surface brightness irregularity, as seen in the Coma and Ophiuchus clusters (Watanabe et al. 1999, 2001); moreover, X-ray emissions are more concentrated in the center. This means that this cluster has not experienced recent merger activity. Therefore, direct shock heating via a major merger does not account for this structure. It is partly plausible that hot regions

associated with point sources would be caused by the energy output of the AGN activity.

On the other hand, cool regions could be explained by the contribution of infalling groups of galaxies not yet thermalized. In the outer envelope the contribution of this component is significant to decrease the temperature of the main body of a cluster. On the contrary, the large difference in the temperature is not significantly recognized in the central region. In this case, a somewhat higher temperature in the boundary region is caused by adiabatic compression of the surrounding intracluster gas when the groups of galaxies infall to the main body of a cluster.

There is always a large cD galaxy at the center of massive cooling flow clusters, and around 71% of all cD galaxies in cooling flows show evidence of radio activity (Burns 1990). Böhringer et al. (2002) finds that the power of the AGN jets from radio sources is more than sufficient to heat the cooling flows and to reduce the mass-deposition rates. In the case of A 1650, because it hosts a radio-quiet cD galaxy and the X-ray emission is more peaked, we expect a massive cooling flow. While the temperature of the ICM slightly drops even in the central 0'25 of the cluster, the addition of a cooling flow component does not improve the fits. Thus, A 1650 bears no evidence of multiphase gas, refuting an earlier imaging study of $\dot{M} \sim 200 M_{\odot} \text{ yr}^{-1}$ (Peres et al. 1998). We suggest that adiabatic heating via infalling of groups is sufficient to heat the cooling flow and to reduce the mass-deposition rate.

8. Conclusion

The non-uniform distribution of the temperature and abundance in an angular extent of 10' (1.4 Mpc) in A 1650 was obtained by a spectral analysis in 19 systematically-subdivided regions and in the specified regions referred to the hardness ratio (HR) map with bin sizes of 17''6. The value of HR is a useful indicator to investigate the spatial variation of the spectral feature. The average temperature and abundance were obtained to be $5.62^{+0.05}_{-0.07}$ keV and $0.36^{+0.02}_{-0.01}$ solar within a radius of 5', respectively, where the redshift was derived to be $8.01^{+0.02}_{-0.02} \times 10^{-2}$ against an optical value of 8.45×10^{-2} . It turned out that cool and hot regions with a temperature of 4–6 keV and a scale-length of a few 100 kpc are patchily distributed in the outer envelope, whereas the radially increasing temperature and decreasing abundance are significantly observed in the central core region. This temperature structure could be explained by the infalling group of galaxies to the main body of the cluster. In the outskirts of A 1650 the spectrum of the Galactic diffuse emissions was obtained with significant detection of O VII and O VIII lines. Moreover, this cluster extends to a radius of 10', where we found more than 30 point sources. Their association with the cluster is still an open question, since their distances are not well-defined.

We thank an anonymous referee for a careful reading of the manuscript and helpful comments. This work was based on observations obtained with XMM-Newton, an ESA science mission with instruments and contributions directly funded by ESA member states and USA (NASA). This work was supported in part by a Grant-in-Aid for Specially Promoted Research contract 07102007, from the Ministry of Education, Culture, Sports, Science and Technology.

References

- Abell, G. O., Corwin, H. G., Jr., & Olowin, R. P. 1989, *ApJS*, 70, 1
- Anders, E., & Grevesse, N. 1989, *Geochim. Cosmochim. Acta*, 53, 197
- Arnaud, M., Neumann, D. M., Aghanim, N., Gastaud, R., Majerowicz, S., & Hughes, J. P. 2001, *A&A*, 365, L80
- Bagchi, J., & Kapahi, V. K. 1994, *J. Astrophys. Astr.*, 15, 275
- Böhringer, H., Matsushita, K., Churazov, E., Ikebe, Y., & Chen, Y. 2002, *A&A*, 382, 804
- Burns, J. O. 1990, *AJ*, 99, 14
- Ciliegi, P., Bassani, L., & Caroli, E. 1995, *ApJ*, 439, 80
- De Grandi, S., & Molendi, S. 2001, *ApJ*, 551, 153
- Dickey, J. M., & Lockman, F. J. 1990, *ARA&A*, 28, 215
- Furusho, T., Yamasaki, N. Y., Ohashi, T., Shibata, R., & Ezawa, H. 2001, *ApJ*, 561, L165
- Hayakawa, S., Kato, T., Nagase, F., Yamashita, K., & Tanaka, Y., 1978, *A&A*, 62, 21
- Ikebe, Y., Reiprich, T. H., Böhringer, H., Tanaka, Y., & Kitayama, T. 2002, *A&A*, 383, 773
- Irwin, J. A., & Bregman, J. N. 2001, *ApJ*, 546, 150
- Jansen, F., et al. 2001, *A&A*, 365, L1
- Kaastra, J. S. 1992, *An X-Ray Spectral Code for Optically Thin Plasmas* (Internal SRON-Leiden Report, updated version 2.0)
- Kaastra, J. S., Ferrigno, C., Tamura, T., Paerels, F. B. S., Peterson, J. R., & Mittaz, J. P. D. 2001, *A&A*, 365, L99
- Liedahl, D. A., Osterheld, A. L., & Goldstein, W. H. 1995, *ApJ*, 438, L115
- Markevitch, M., et al. 2000, *ApJ*, 541, 542
- Markevitch, M., Forman, W. R., Sarazin, C. L., & Vikhlinin, A. 1998, *ApJ*, 503, 77
- Mewe, R., Gronenschild, E. H. B. M., & van den Oord, G. H. J. 1985, *A&AS*, 62, 197
- Mewe, R., Lemen, J. R., & van den Oord, G. H. J. 1986, *A&AS*, 65, 511
- Nandra, K., & Pounds, K. A. 1994, *MNRAS*, 268, 405
- Nevalainen, J., Lieu, R., Bonamente, M., & Lumb, D. 2003, *ApJ*, 584, 716
- Peres, C. B., Fabian, A. C., Edge, A. C., Allen, S. W., Johnstone, R. M., & White, D. A. 1998, *MNRAS*, 298, 416
- Ricker, P. M. 1998, *ApJ*, 496, 670
- Roettiger, K., & Flores, R. 2000, *ApJ*, 538, 92
- Roettiger, K., Loken, C., & Burns, J. O. 1997, *ApJS*, 109, 307
- Sanders, J. S., & Fabian, A. C. 2001, *MNRAS*, 325, 178
- Sanders, J. S., & Fabian, A. C. 2002, *MNRAS*, 331, 273
- Snowden, S. L., et al. 1995, *ApJ*, 454, 643
- Spitzer, L., Jr. 1962, *Physics of Fully Ionized Gases* (New York: Interscience)
- Struble, M. F., & Rood, H. J., 1999, *ApJS*, 125, 35
- Strüder, L., et al. 2001, *A&A*, 365, L18

Tamura, T., et al. 2001, *A&A*, 365, L87

Turner, M. J. L., et al. 2001, *A&A*, 365, L27

Watanabe, M., Yamashita, K., Furuzawa, A., Kunieda, H., &
Tawara, Y. 2001, *PASJ*, 53, 605

Watanabe, M., Yamashita, K., Furuzawa, A., Kunieda, H.,
Tawara, Y., & Honda, H. 1999, *ApJ*, 527, 80

White, D. A. 2000, *MNRAS*, 312, 663

White, D. A., Jones, C., & Forman, W. 1997, *MNRAS*, 292,
419